PHYSICS

First-passage statistics of colloids on fractals: Theory and experimental realization

Christoph Zunke[1], Jörg Bewerunge[1], Florian Platten[1,2], Stefan U. Egelhaaf[1], Aljaž Godec[3]*

In nature and technology, particle dynamics frequently occur in complex environments, for example in restricted geometries or crowded media. These dynamics have often been modeled invoking a fractal structure of the medium although the fractal structure was only indirectly inferred through the dynamics. Moreover, systematic studies have not yet been performed. Here, colloidal particles moving in a laser speckle pattern are used as a model system. In this case, the experimental observations can be reliably traced to the fractal structure of the underlying medium with an adjustable fractal dimension. First-passage time statistics reveal that the particles explore the speckle in a self-similar, fractal manner at least over four decades in time and on length scales up to 20 times the particle radius. The requirements for fractal diffusion to be applicable are laid out, and methods to extract the fractal dimension are established.

INTRODUCTION

A fractal is a self-similar geometrical object that appears identical on all observed length scales (*1*). Concepts of fractal geometry (*1*) and the related percolation (*2*) are deeply ingrained in the theoretical description of transport and diffusion in complex media (*3*). Diffusion and transport in fractal spaces (*4*, *5*) have been applied to a diverse range of processes and systems, including fracture networks (*6*), porous media (*7*), disordered alloys (*8*), structured surfaces (*9*), cellular cytoplasm (*10*–*12*), plasma membranes (*13*, *14*), and chromatin (*15*, *16*). For the organization of chromatin, a fractal structure plays a particularly important role; the fractal packaging is believed to facilitate long-range enhancer-promoter interactions and thereby control gene transcription (*17*, *18*) through a complex interplay between packing and transcription (*18*). In addition, the conformational dynamics of proteins has been linked to the fractal-like structure of configuration space (*19*). Moreover, the confinement to a fractal space has important and nontrivial consequences for transport-dependent processes. For example, in diffusion-dominated chemical reactions and ligand binding, such as occurring in the chromatin system, the (fractal) geometry of the surrounding space determines whether molecules explore this space recurrently or transiently, which in turn determines, e.g., the dependence of the reaction rate on the concentration or initial separation of reactant molecules (*3*, *20*).

Diffusion on a fractal is often inferred because structural data (*7*, *8*, *21*, *22*) or transiently anomalous diffusion (*3*, *15*, *16*, *23*) suggests a fractal structure of the medium. However, a solid physical basis for invoking fractal concepts is often missing because of ambiguous predictions of diffusion models. Because fractals cover multiple spatial scales, a conclusive inference of a fractal structure and its fractal dimension requires an elaborate multimodal approach (*18*) that integrates tomography (*24*), superresolution microscopy (*25*, *26*), spectroscopic imaging (*27*), and computational methods (*28*). To avoid or resolve controversies without resorting to such complex endeavors, the grand long-term aim is to establish a "toolbox" for disentangling the microscopic origins of anomalous dynamics (*10*, *29*–*31*). This can be provided by first-passage observables, which characterize the first instance a diffusing particle reaches some predefined destination (*20*, *32*–*35*). They are typically very sensitive to the underlying transport mechanism (*36*, *37*). In particular, they have been shown to successfully discriminate diffusion on fractal objects from other types of dynamics (*37*). Nevertheless, first-passage time distributions are rarely measured in experiments and are only slowly emerging as powerful experimental observables (*38*, *39*), which have not yet been applied to fractals.

In contrast to the very complex environments, for example, inside living cells (*10*–*16*, *40*), and the difficulty to follow individual atoms and molecules, colloidal particles in external potentials represent an ideal model system. Because of their high susceptibility to external fields, colloidal particles can be precisely manipulated by, e.g., light (*41*–*46*), electrical and magnetic fields (*41*, *47*–*49*), or microfluidic devices (*50*). Furthermore, their response to an external field can be followed on all relevant length scales, i.e., from the microscopic level of individual particles to the macroscopic bulk behavior of many particle systems. Thus, colloidal particles in a well-defined fractal environment with a tunable fractal dimension promise to be a powerful model system for systematic, quantitative studies.

Here, we present such a system. Micrometer-sized colloidal particles moving in a quasi–two-dimensional plane were exposed to a laser speckle pattern (*43*, *51*–*54*) whose random structure has been linked to fractals (*55*). Whereas the arrangement of the particles has been addressed previously (*54*), we now investigate the particle dynamics. The particles were followed by optical microscopy (Fig. 1A), and, instead of the usual mean squared displacement, we focused on the first-passage statistics. This revealed that a particle explores the speckle pattern in a self-similar, fractal manner at least over four orders of magnitude in time and on length scales at least 8 to 20 times the particle radius.

After performing the experiments, we developed a theoretical explanation for the observed fractal exploration of the speckle pattern based on the assumption that the particle remains confined to high-intensity regions (Fig. 1B). The largest connected high-intensity region is shown to display a self-similar structure. As will be shown below, its (Minkowski) fractal dimension, d_f, can be continuously

[1]Condensed Matter Physics Laboratory, Heinrich Heine University, Universitätsstrasse 1, 40225 Düsseldorf, Germany. [2]Institute of Biological Information Processing, Biomacromolecular Systems and Processes (IBI-4), Forschungszentrum Jülich, 52425 Jülich, Germany. [3]Mathematical bioPhysics Group, Max Planck Institute for Biophysical Chemistry, 37077 Göttingen, Germany.
*Corresponding author. Email: agodec@mpibpc.mpg.de

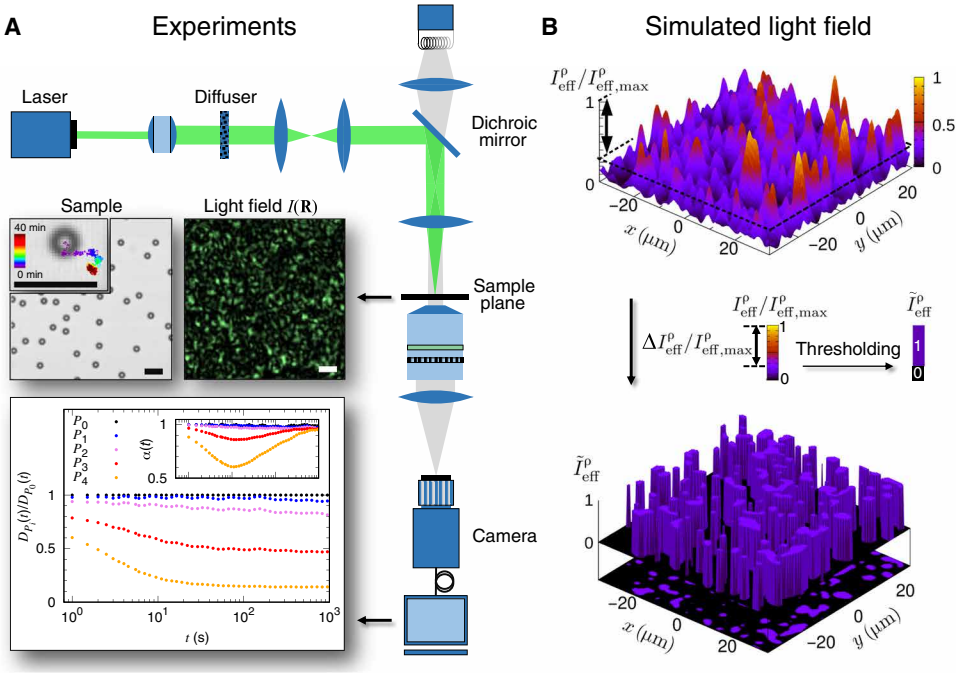

Fig. 1. Experimental setup and example of an effective intensity pattern experienced by a particle. (**A**) Schematic of the experimental setup as well as part of an experimentally realized speckle pattern $I(\mathbf{R})$ (green) and part of a typical image of the sample with the inset depicting a typical trajectory in the presence of a light field with laser intensity P_4. Scale bars, 10 μm. Bottom: Effective diffusion coefficient $D_{P_i}(t) \equiv \mathrm{d}\langle \overline{\delta R^2}(t) \rangle / 4\mathrm{d}t$ normalized by the effective diffusion coefficient in the absence of a light field, $D_{P_0}(t)$, and in the inset the "anomalous exponent" $\alpha(t) \equiv \mathrm{d}\ln\langle \overline{\delta R^2}(t) \rangle / \mathrm{d}\ln t$, in the absence ($P_0$) and presence of a light field $I(\mathbf{R})$ (where the laser intensity increases from P_1 to P_4). (**B**) Example of (top) a simulated effective intensity $I^{\rho}_{\mathrm{eff}}(\mathbf{R})$ corresponding to the experimentally realized speckle pattern $I(\mathbf{R})$ integrated over a particle of radius $\rho = 1.4\,\mu\mathrm{m}$. The effective intensity is normalized by the maximum effective intensity $I^{\rho}_{\mathrm{eff,max}}$. The arrow denotes $\Delta I^{\rho}_{\mathrm{eff}}/I^{\rho}_{\mathrm{eff,max}}$ used for thresholding. Bottom: Thresholded (binary) effective intensity $\tilde{I}^{\rho}_{\mathrm{eff}}(\mathbf{R})$, which indicates areas with low intensity [$I^{\rho}_{\mathrm{eff}}(\mathbf{R}) < I^{\rho}_{\mathrm{eff,max}} - \Delta I^{\rho}_{\mathrm{eff}}$, represented by a value of 0] and high intensity [$I^{\rho}_{\mathrm{eff}}(\mathbf{R}) \geq I^{\rho}_{\mathrm{eff,max}} - \Delta I^{\rho}_{\mathrm{eff}}$, represented by a value of 1]. It is also displayed in a two-dimensional representation (bottom). The particles are assumed to diffuse in areas of uniform high intensity (purple areas) and to not enter the low-intensity (black) areas. The high-intensity areas represent fractal clusters displaying a self-similar, fractal structure whose fractal dimension depends on the laser power.

adjusted by increasing the laser power. Within the investigated range, a linear relationship between the laser power and d_f is observed and corroborated qualitatively by our computer simulations. We discuss the relevance of our results and illustrate it by the fractal packaging of chromatin and its consequences for transcription regulation. Our experimental realization represents a versatile and controllable platform for probing particle arrangements (*54*) and, as shown here, particle dynamics on a fractal structure. It offers novel opportunities for systematic investigations of effective diffusion in fractal spaces.

RESULTS

Experimental characterization of the dynamics in speckle patterns

A dilute aqueous suspension of polystyrene spheres with radius $\rho = 1.4\,\mu\mathrm{m}$ was investigated. These moved in a quasi–two-dimensional plane at the bottom of the sample cell because of the density mismatch with water and the radiation pressure. The particles were exposed to laser speckles generated by illuminating a diffuser with an expanded laser beam (Fig. 1A; see Materials and Methods for details on the samples and setup). This imposed an external potential on the particles (*54*). While the particles explored the speckle pattern, they were observed with an inverted microscope. From the images, particle positions were extracted, and particle trajectories $\mathbf{R}(t)$ were reconstructed (*56*).

In experiments, typically the so-called ensemble and time-averaged mean squared displacement of a particle $\langle \overline{\delta R^2}(t) \rangle = [N(T-t)]^{-1} \sum_{i=1}^{N} \int_0^{T-t} [\mathbf{R}_i(t'+t) - \mathbf{R}_i(t')]^2 \mathrm{d}t'$ is determined, i.e., the squared relative displacement of the particle within a lag time t averaged over a long trajectory of duration T as well as over trajectories of different particles (*57*). At short lag times, $\langle \overline{\delta R^2}(t) \rangle$ displays a normal, $\langle \overline{\delta R^2}(t) \rangle \propto t$, and at intermediate lag times, a transiently subdiffusive scaling, $\langle \overline{\delta R^2}(t) \rangle \propto t^{\alpha}$ with $\alpha < 1$. It again turns normal $\langle \overline{\delta R^2}(t) \rangle \propto t$ once the particle has explored larger areas of the quenched laser speckle (*58*). Correspondingly, the effective diffusion coefficient $D_P(t) \equiv \mathrm{d}\langle \overline{\delta R^2}(t) \rangle / 4\mathrm{d}t$ is constant at short times, decreases at intermediate times, and again is constant at long times with a value $D_P(t \to \infty)$ that decreases with increasing laser power P (Fig. 1A, bottom). The full span of scaling is quantified in terms of the "anomalous exponent" $\alpha(t) \equiv \mathrm{d}\ln\langle \overline{\delta R^2}(t) \rangle / \mathrm{d}\ln t$ that starts with, and at long time converges to, 1, i.e., $\alpha(t=0) = \alpha(t \to \infty) = 1$, whereas $\alpha(t) < 1$ at intermediate times (Fig. 1A, bottom).

Instead of $\langle \overline{\delta R^2}(t) \rangle$, we focus on the first-passage time statistics. On the basis of the trajectories, we determined the first-passage time τ_R, which is defined as the first instance in time the particle is displaced a distance R from its original location $\mathbf{R}(0)$, i.e., $\tau_R \equiv \min_t \{ |\mathbf{R}(t) - \mathbf{R}(0)| = R \}$. The mean first-passage time $\langle \tau_R \rangle$ is shown as a function of the displacement R and for different laser powers P in Fig. 2A. With increasing laser power P, the mean first-passage time $\langle \tau_R \rangle$ increases, indicating a slowing down of the dynamics, as expected. Furthermore, $\langle \tau_R \rangle$ also

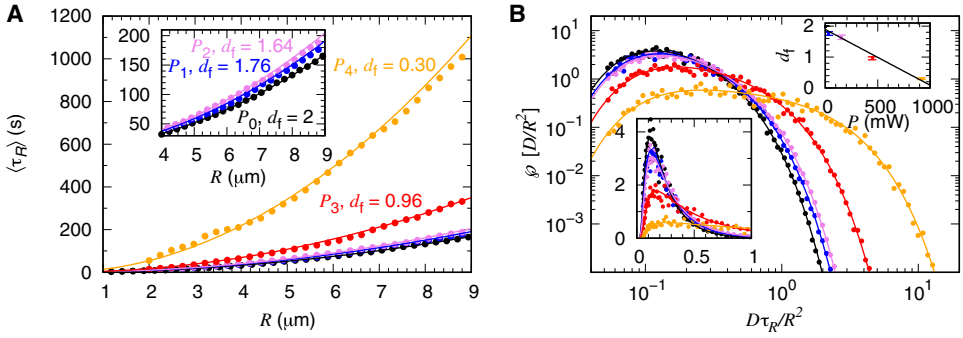

Fig. 2. First-passage time statistics. (**A**) Mean first-passage time $\langle\tau_R\rangle$ required for a displacement R, while the particle is exposed to a speckle pattern created using different values of the laser power P (symbols); the inset shows a magnification for low P. The laser powers are $P_0 = 0$ mW, $P_1 = 34$ mW, $P_2 = 155$ mW, $P_3 = 446$ mW, and $P_4 = 917$ mW. The fractal dimension d_f was determined by fitting Eq. 1 to the experimental data (lines). (**B**) Probability density of the first-passage time $\wp(\tau_R)$ showing a collapse of the experimental probability densities for all R onto a P-dependent master curve (symbols) and predictions based on Eq. 2 (lines). Inset bottom left: Short-time behavior of $\wp(\tau_R)$ on a linear scale. Inset top right: Fitted fractal dimension d_f (symbols) as a function of the laser power P and corresponding linear fit (line). The error bars reflect the uncertainty of the estimated d_f (see Materials and Methods for details).

increases with increasing displacement R. The results in Fig. 2A suggest a scaling $\langle\tau_R\rangle \propto R^2$ in agreement with the universal scaling of diffusive Markov processes (*59*). Using this scaling, for each laser power P, the probability density of the first-passage time $\wp(\tau_R)$ can be collapsed onto a single master curve irrespective of R (Fig. 2B, symbols). The collapsed probability density broadens and moves to larger first-passage times τ_R with increasing laser power P.

Theory of first-passage statistics in fractal media

For a theoretical description of the particle motion, the generalized (mean field) diffusion equation was adopted (*4*, *5*). The generalized diffusion equation was shown to adequately describe first-passage statistics for random walks on deterministic fractals, such as a Sierpinski gasket and T graph, as well as on (random) critical percolation clusters for a broad range of system sizes including small systems (*20*). To describe the experiments, the particles were assumed to diffuse on an isotropic random fractal with hard walls and fractal dimension $0 < d_f \leq 2$ (Fig. 1B). (However, below, we extend the results to higher fractal dimensions and subdiffusion.) We can formulate the statistics of first passage as a two-point boundary value problem, which is analytically solvable (for details, see Materials and Methods). The mean first-passage time $\langle\tau_R\rangle$ can be shown to be given by

$$\langle\tau_R\rangle = \frac{R^2}{2\,d_f D} \tag{1}$$

where D is the particle's bare (short time) diffusion coefficient. In the experiments, the diffusion coefficient D is smaller than the free diffusion coefficient because of the proximity to the coverslip (*60*, *61*). D was experimentally determined in the absence of a speckle pattern ($P = 0$), where $d_f = 2$, which yielded $D \simeq 0.121\ \mu m^2/s$ (Fig. 2A, black symbols and line). With increasing laser power P, the radiation pressure increases and pushes the particles closer to the coverslip, resulting in a further slight decrease in D (see also Fig. 1A, bottom) (*58*). We neglect this effect and assume a value of D that is independent of the laser power P. A fit based on Eq. 1 yields very good agreement with the experimental data (Fig. 2A). This confirms the quadratic scaling of $\langle\tau_R\rangle$ with displacement R. Furthermore, the determined fractal dimension d_f as a function of the laser power P is shown in Fig. 2B (inset top right). Within the explored range, d_f linearly decreases with P.

It is possible to derive the exact probability density function $\wp(\tau_R)$, which reads (for a derivation, see Materials and Methods)

$$\wp(\tau_R) = \frac{4D}{R^2}\sum_{k\geq 1}\frac{(\beta_{\nu,k}/2)^{\nu+1}}{\Gamma(\nu+1)\,J_{\nu+1}(\beta_{\nu,k})}\,e^{-\beta_{\nu,k}^2 D\tau_R/R^2} \tag{2}$$

where $\nu = \nu(d_f) \equiv (d_f/2) - 1$, $\Gamma(x)$ denotes the Gamma function, and $\beta_{\nu,k}$ is the k-th zero of the Bessel function of the first kind and order ν, $J_\nu(z)$, that is, $J_\nu(\beta_{\nu,k}) = 0$. The result in Eq. 2 appears to not have been derived before and holds for any fractal dimension between 0 and d, the Euclidean embedding dimension of physical space. It also shows a quadratic scaling with the displacement R, which implies that by rescaling first-passage times according to $\tau_R \to \tau_R D/R^2$ (which is equivalent to expressing τ_R in units of R^2/D), all data corresponding to the same fractal dimension d_f should collapse onto a single master curve. This collapse is confirmed to a remarkable agreement (Fig. 2B), although it does not involve any free parameter or fitting. These results therefore suggest that, as hypothesized, the particles explore the speckle pattern in a self-similar, fractal manner and that the diffusion coefficient is, to a good approximation, independent of the laser power. However, they explain neither the origin of the fractal scaling nor the dependence of the determined fractal dimension d_f on laser power P (Fig. 2B, inset top right), which we will address in the following.

Theoretical analysis of the geometry of speckle patterns

To gain a better understanding of these observations, the statistics of the speckle patterns were inspected. For an ideal speckle pattern $I(\mathbf{R})$ with average intensity $\bar{I} \propto P$, the local intensities are statistically independent, exponentially distributed random variables with probability density $p(I) = e^{-I/\bar{I}}/\bar{I}$ (*51*). The colloidal particle is susceptible to electromagnetic radiation because its optical properties are different from those of the suspending liquid (*44*, *45*). The particle's finite volume is taken into account by integrating over its cross section weighted by the projected volume (*52*)

$$I_{\text{eff}}^{\rho}(\mathbf{R}) \simeq \frac{3}{2\pi\rho^2}\int_{|\mathbf{x}|\leq\rho} d\mathbf{x}\, I(\mathbf{R}+\mathbf{x})\sqrt{1-(|\mathbf{x}|/\rho)^2} \tag{3}$$

Then, a point-like particle in the effective intensity pattern $I_{\text{eff}}^{\rho}(\mathbf{R})$ can be considered instead of a finite particle with radius ρ moving

in a speckle pattern $I(\mathbf{R})$. We took a square grid of 201 × 201 pixels and implemented periodic boundary conditions to mimic an infinite system. To each point $\mathbf{R}$, an independent random intensity $I(\mathbf{R})$ drawn from an exponential distribution was assigned and then the effective intensity $I^{\rho}_{\mathrm{eff}}(\mathbf{R})$ was calculated according to Eq. 3. Two particular realizations of the effective intensity $I^{\rho}_{\mathrm{eff}}(\mathbf{R})$ in the case of ρ = 3 pixels and two different laser powers P are shown in Fig. 3 (A and B, left panels).

It is postulated that at all times, the particle remains within a high-intensity region. These high-intensity regions are defined as all locations $\mathbf{R}_{\mathrm{hi}}$ whose effective intensity $I^{\rho}_{\mathrm{eff}}(\mathbf{R}_{\mathrm{hi}})$ is within some appropriately chosen range $\Delta I^{\rho}_{\mathrm{eff}}$ of $I^{\rho}_{\mathrm{eff,max}} \equiv \max_{\mathbf{R}} I^{\rho}_{\mathrm{eff}}(\mathbf{R})$, the maximum for a given (random) realization of $I^{\rho}_{\mathrm{eff}}(\mathbf{R})$. Hence, $I^{\rho}_{\mathrm{eff}}(\mathbf{R}_{\mathrm{hi}})$ lies between $I^{\rho}_{\mathrm{eff,max}} - \Delta I^{\rho}_{\mathrm{eff}}$ and $I^{\rho}_{\mathrm{eff,max}}$. The range $\Delta I^{\rho}_{\mathrm{eff}}$ was taken to be identical for all P and all realizations of $I^{\rho}_{\mathrm{eff}}(\mathbf{R})$. It quantifies the maximum intensity fluctuation within the high-intensity regions, which was assumed to be negligible or to become locally averaged out. More precisely, each realization of the thresholded (binary) effective intensity was determined as

$$\tilde{I}^{\rho}_{\mathrm{eff}}(\mathbf{R}) = \theta(I^{\rho}_{\mathrm{eff}}(\mathbf{R}) + \Delta I^{\rho}_{\mathrm{eff}} - I^{\rho}_{\mathrm{eff,max}}) \quad (4)$$

where $\theta(x)$ is the Heaviside step function that is equal to 1 whenever $x \geq 0$ and 0 otherwise. This procedure resulted in a binary intensity pattern (Fig. 3, A and B, middle) (*62*). Depending on the mean speckle intensity $\bar{I}$, such thresholding produced finite and/or percolating regions. In either case, once a particle is equilibrated, it will most likely be found in the largest region (Fig. 3, A and B, right).

For several particle radii ρ and laser powers P, 10^5 realizations of a speckle pattern were created, and this procedure was applied. Subsequently, the Minkowski fractal dimension d_f of the largest high-intensity region was determined by box counting. The number of boxes required to cover the largest high-intensity region was averaged over all realizations to yield $\langle N \rangle$. This number scaled with the inverse box size $\epsilon = 1/L$ according to a power law $\langle N \rangle \propto \epsilon^{d_f}$ and hence allowed us to determine the fractal dimension d_f. The results for ρ = 3 pixels are shown in Fig. 3C. They indicate a self-similar structure of the largest high-intensity region on a scale of up to 20 particle radii for all laser powers P (the upper limit may depend on the particle radius because a corresponding increase in the system size is precluded by computational limitations). Moreover, with increasing mean intensity $\bar{I}$ and hence laser power P, the fractal dimension d_f was found to decrease (Fig. 3, C and D) in qualitative agreement with the experimental results (Fig. 2B, inset to right). For each particle radius, we observed a regime of the laser power P where d_f decays linearly with P (Fig. 3D). This may explain the linear dependence observed in the experimentally explored range (Fig. 2B, inset top right).

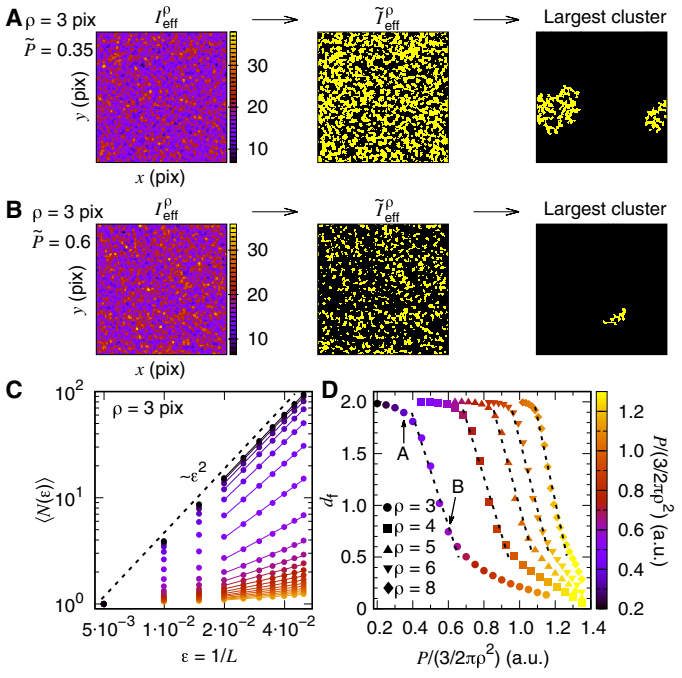

Fig. 3. Fractal geometry of the thresholded high-intensity regions of the speckle pattern. The effective intensity field $I^{\rho}_{\mathrm{eff}}(\mathbf{R})$ was generated according to Eq. 3 for a particle radius ρ = 3 pixels and a scaled laser power in arbitrary units (**A**) $\tilde{P} \equiv P/(3/2\pi\rho^2) = 0.35$ and (**B**) 0.6 (left; see Fig. 1B, top). All intensities within a range $\Delta I^{\rho}_{\mathrm{eff}}$ of the maximum intensity $I^{\rho}_{\mathrm{eff,max}}$ were set to 1 and all others to 0 to yield the thresholded (binary) effective intensity $\tilde{I}^{\rho}_{\mathrm{eff}}(R)$ (middle; see Fig. 1B, bottom), and the largest high-intensity region was selected for further analysis (right). The area corresponds to 201 × 201 pixels. (**C**) Minkowski (box-counting) analysis was used to determine the scaling of the average number of boxes $\langle N \rangle$ of size L required to cover the largest high-intensity region as a function of the inverse box size $\epsilon = 1/L$. The average was taken over 10^5 realizations of the speckle pattern and the corresponding effective intensity pattern for a particle with radius ρ = 3 pixels. The fractal dimension d_f was extracted from the power-law scaling $\langle N \rangle \propto \epsilon^{d_f}$ for sufficiently large L for different values of the laser power P. (**D**) Fitted fractal dimension d_f as a function of normalized laser power for particles of radii ρ = 3, 4, 5, 6, and 8 pixels (symbols), respectively, with the dashed lines indicating an approximately linear decay in qualitative agreement with experiments. The uncertainty of the fit was much smaller than the size of the symbols. Arrows denote conditions (ρ and P) presented in (A) and (B). a.u., arbitrary units.

DISCUSSION

We have presented a systematic and quantitative analysis of first-passage time statistics of colloidal particles in speckle patterns. The particles explored the speckle pattern in a self-similar, fractal manner on a length scale of 8 to 20 particle radii. The effective fractal dimension d_f was shown to depend linearly on the laser power P within the examined range of P. A remarkable agreement was found between theory and experiments, as evidenced in Fig. 2B by the collapse of experimental first-passage statistics onto the theoretical prediction in Eq. 2 as well as the observed linear dependence of d_f on the laser power P (compare Figs. 2B, inset top right, and 3D). This is despite the simplifying assumption that the particles remain confined to high-intensity regions of the speckle pattern and hence explore a fractal region that is delimited by "hard walls." This is not strictly fulfilled in the experiments (Figs. 1B and 3, A and B), which suggests that the fractal regions need not be confined by hard walls as assumed in the theoretical description, but "soft walls" may lead to very similar first-passage kinetics. This could have important consequences for the interpretation of single-particle tracking experiments inside living cells (*12*–*16*), where often hard wall fractals are thought to be required in order for the dynamics to display fractal-like statistics (*15*, *16*, *21*, *22*).

The agreement between experiment and theory implies that the diffusion of particles in the laser speckle is normal, which, strictly speaking, is not the case, at least not on all time scales [see Fig. 1A, bottom, and (*58*, *63*) showing transient subdiffusion]. The effective

intensity pattern experienced by a point-like particle, $I^{\rho}_{\mathrm{eff}}(\mathbf{R})$ (Fig. 1B), has values that are generally Gamma distributed, in the present case almost Gaussian distributed, and have a spatial correlation length λ determined by the particle radius ρ and the speckle size; in the present experiments, λ is similar to ρ (*52*). The short-time diffusion on length scales much smaller than the correlation length λ may throughout be assumed to be normal (Fig. 1A, bottom). Conversely, on length scales sufficiently large compared to λ, the particle explores many distinct high-intensity regions that represent different fractals whose positions are quenched in space. Thus, the motion along a single trajectory becomes self-averaging and, hence, the observed long-time diffusion normal, where the effective diffusion coefficient $D_P(t)$ depends on the laser power P [see Fig. 1A, bottom, and (*63*, *64*) for a thermodynamical argument].

When investigating the first-passage observables, by construction, we are interested in time scales during which the particle remains within the same high-intensity region and ask for the first-passage time within this region. Therefore, the particle explores only areas in the vicinity of the particle's location at time $t = 0$. In particular, by probing first-passage times, the particle's trajectories are terminated once the absolute displacement reaches a given value R. The dynamics along an individual trajectory is thus a priori not expected to be self-averaging over several high-intensity regions within a quenched realization of the speckle. On the time scales during which the particle explores a region with a linear dimension from 8 to 20 times the particle radius (depending on the laser power P), the dynamics effectively evolves as normal diffusion within a fractal space. The average over disorder, i.e., different realizations of the speckle pattern, then takes into account the different shapes, sizes, and intensities of individual high-intensity regions.

These characteristics of the first-passage analysis are important for a comparison of the present findings with results obtained by complementary methods probing dynamics on distinct time scales, e.g., fluorescence correlation spectroscopy revealing pronounced subdiffusion (*12*). In particular, first-passage observables probe properties that a priori are different from the ones encoded in the mean squared displacement. Nevertheless, if the particles follow a self-averaging trajectory in the high-intensity regions for most of the time, i.e., the time spent outside of a high-intensity region can be considered to be negligible, then the effective long-time diffusion coefficient $D_P(t\to\infty)$ (Fig. 1A) might be related to the fractal dimension d_f according to $\overline{\langle \delta R^2 \rangle} \simeq 2d\,D_P(t\to\infty)\,t \approx 2\widetilde{d}_f D_{P_0} t$, where D_{P_0} is the bare diffusion coefficient for $P = 0$ and d is the Euclidean (embedding) dimension of the physical space. This comparison yields the fractal dimension $\widetilde{d}_f = d\,D_P(t\to\infty)/D_{P_0}$. In our case with $d = 2$, therefore, $\widetilde{d}_f/2$ can be read off as $D_P(t)/D_{P_0}$ at long times $t \to \infty$, as shown in Fig. 1A. The fractal dimension $\widetilde{d}_f$ depends only on the ratio of $D_P(t\to\infty)/D_{P_0}$ and not on the individual values. The fractal dimension $\widetilde{d}_f$ agrees very well with d_f derived from the first-passage analysis in Fig. 2 (see table S1). This suggests that the above condition is fulfilled. Note, however, that this comparison will yield a "fractal dimension" in any system displaying asymptotically normal diffusion irrespective of the underlying dynamics. Therefore, only after it has been established that the dynamics can be described as diffusion on a fractal, one can conveniently infer the fractal dimension from the long-time diffusion coefficient $D_P(t\to\infty)$.

It is established that one can use first-passage observables to probe, e.g., the origins of anomalous diffusion (*37*). Our present methodology, in particular the analysis summarized in Fig. 2, in addition allows us to infer whether a system's dynamics can, on a given spatial and temporal scale, effectively be described as diffusion on a fractal. For this to be the case, two conditions need to be fulfilled: (i) The mean first-passage time must scale quadratically with R, and (ii) rescaled first-passage times $\tau_R \to \tau_R D/R^2$ must collapse (in some appropriate range of R) onto a single master curve described by Eq. 2 with a fractal dimension d_f extracted from Eq. 1. Here, some additional remarks are in order. First, the results in Eq. 2 are not limited to $d_f \le 2$ but, in fact, hold for any $0 < d_f \le d$. Second, our results can accommodate for subdiffusion with a so-called "walk dimension" $d_w \ge 2$ and an anomalous diffusion coefficient D_w, i.e., $\overline{\langle \delta R^2 \rangle} \propto D_w t^{2/d_w}$ (*3*). The corresponding mean first-passage time reads (for details, see Materials and Methods)

$$\langle \tau_R \rangle = \frac{R^{d_w}}{d_w(d_f + 1 - d_w/2)\,D_w} \tag{5}$$

whereas Eq. 2 modifies to

$$\wp(\tau_R) = \frac{d_w^2 D_w}{R^{d_w}} \sum\nolimits_{k\ge 1} \frac{(\beta_{\mu,k}/2)^{\mu+1}}{\Gamma(1+\mu)\,J_{\mu+1}(\beta_{\mu,k})} \mathrm{e}^{-d_w^2 \beta_{\mu,k}^2 D_w \tau_R / 4R^{d_w}} \tag{6}$$

where $\mu = (d_f + 1)/d_w - 3/2$, which amounts to rescaling the first-passage time $\tau_R \to \tau_R d_w^2 D_w / 4R^{d_w}$ to achieve the aforementioned collapse. For $d_w = 2$ Eqs. 5 and 6 reduce to Eqs. 1 and 2, respectively. Third, sufficient statistics must be collected for every value of R to prevent finite-time effects, as described in Materials and Methods, or the range of R values must be adjusted accordingly. Fourth, there may exist also a nonzero lower threshold of R values. Hence a fractal description does not necessarily extend to arbitrarily small scales. Fifth, a finite temporal resolution may introduce artifacts when first-passage times are short. Last, the presence of anomalous diffusion with $d_w > 2$ introduces an additional fitting parameter that may potentially lead to overfitting and/or uncertainties.

Inferring whether the kinetics of a process are substantially affected or controlled by the fractal structure of the medium is relevant for many systems, as mentioned in the Introduction. It seems to be particularly important in the context of gene regulation—the random search of transcription factors for target genes on chromatin (*15*, *16*, *20*, *32*, *65*–*67*). Namely, whenever $d_f < d_w$ (this includes Brownian motion with $d_w = 2$ in fractal dimensions $d_f < 2$), the random search process is recurrent. In this case, the initial distance to the target gene decisively controls the search kinetics, rendering the colocalization of coregulated genes kinetically favorable (*20*, *32*). In contrast, when $d_f > d_w$ (such as in the case of Brownian motion in fractal dimensions $d_f \ge 2$), the initial distance to the target gene has only a weak effect, making colocalization kinetically irrelevant (*20*, *32*). According to the most recent and most accurate results (*18*), the fractal dimension of chromatin displays a double scaling, with $d_f \approx 2.6$ on a length scale of 6 to 50 nm and $d_f \approx 3$ on a length scale beyond approximately 102 nm, while the distance between colocalized genes is smaller than approximately 100 nm (i.e., the size of a transcription factory) (*68*). Particle-tracking experiments in the cell nucleus further revealed subdiffusion with a walk dimension $2 \le d_w \le 3$ (*15*, *69*, *70*). Because $d_f \approx 2.6$ is quite close to the Euclidean embedding dimension $d = 3$, the complementary volume surrounding chromatin is likely to be fractal as well (although its precise fractal dimension, in general, depends on the upper length scale of fractal scaling) (*71*). This suggests, irrespective of whether the search process occurs on chromatin or in the surrounding space, that the

dynamics may be recurrent, which would render gene colocalization kinetically effective (*20*, *32*). Moreover, transcription factors may transiently bind to, and slide on, chromatin, which can additionally enhance the molecular search kinetics (*66*).

As illustrated with our experiments and theoretical description, the experimental setup provides a controlled platform for probing diffusion on a random fractal whose fractal dimension d_f can be tuned easily. Moreover, since the individual particles can be followed, any parameter can be determined, in particular first-passage times. The experiments may be extended to various other situations, for example, colloidal particles with other properties, such as a size different from the speckle size (*52*), a nonspherical shape (*72*), or activity (*73*), or also different objects, such as bacteria (*74*) or microorganisms (*75*). Furthermore, the speckle pattern can be modified (*76*) or made time dependent (*77*), or a directed flow can be superimposed (*6*). Thus, this approach offers new opportunities to systematically and quantitatively investigate diffusion on fractal structures and mimic situations encountered in more complex or less accessible situations, such as in natural, atomic, or molecular systems as well as technological applications.

MATERIALS AND METHODS

Experimental setup, particle tracking, and determination of first-passage times

Dilute aqueous suspensions of colloidal polystyrene spheres with a radius ρ = 1.4 μm and a polydispersity of 3.2% (Interfacial Dynamics Corporation) were prepared. The difference in refractive indices of the particles (n_p = 1.59) and water (n_w = 1.33) allows for trapping. The suspensions were filled into sample cells that were constructed from thoroughly cleaned coverslips and a microscope slide (VWR) assembled to form a small capillary with a height of 170 μm. Because of the density difference between the particles and the solvent as well as the radiation pressure exerted on the particles, the particles were located at the bottom of the capillary. They moved in a quasi–two-dimensional plane with an area fraction of less than 0.08.

A Gaussian beam generated by a solid-state laser (wavelength of 532 nm; Laser Quantum, Opus 532) was expanded and directed to a diffuser (RPC Photonics, Engineered Diffuser EDC-1-A-1r). This resulted in a beam with a macroscopically flat top-hat intensity distribution with fluctuations on a microscopic scale, i.e., a random speckle pattern. This beam was introduced into an inverted microscope and focused in the sample plane (Fig. 1A). The beam illuminated about the field of view. Only trajectories within the light field were considered. The speckle size was comparable to the particle size. The laser was operated with different powers; P_0 = 0 mW, P_1 = 34 mW, P_2 = 155 mW, P_4 = 917 mW, P_5 = 1640 mW, and P_6 = 2600 mW. Only a small fraction of the light reached the sample and was spread over a large area; thus, the power density was very small, and no detectable effect of heating was observed. Details of the optical setup and the speckle pattern have been described previously [condition BE (beam expander) 5× in (*52*)].

The samples were observed using an inverted microscope (Nikon, Eclipse Ti-U) with a 20× extra-long working distance (ELWD) chromatic aberration free infinity (CFI) objective (Nikon, CFI S Plan Fluor ELWD, numerical aperture = 0.45). It was equipped with a complementary metal-oxide semiconductor (CMOS) camera (PixeLINK, PL-B741F), which recorded a field of view of 431 × 345 μm^2. For each laser power P, a sequence of about 10,000 images containing up to 2000 particles was observed with a frame rate of 2 frames/s. From the sequence of recorded images, the particle locations were determined and connected to yield trajectories (*56*).

The first-passage times τ_R to a displacement R were determined on the basis of the trajectories, i.e., by calculating $\tau_R \equiv \min_t\{|\mathbf{R}(t)-\mathbf{R}(0)| = R\}$. The corresponding first-passage time probability density function $\wp(\tau_R)$ and mean first-passage time $\langle\tau_R\rangle$ were then calculated. For each applied laser power P, approximately 1000 to 2000 trajectories $\mathbf{R}(t)$ were analyzed for each displacement R. To avoid spurious correlations, trajectories were not segmented, and hence, the particle positions at the beginning of the recording were the only starting points $\mathbf{R}(0)$ considered. Note that one must assure that the trajectories are long enough to allow for sufficiently many trajectories to reach all considered displacements R. Otherwise, the temporal cutoff leads to artifacts in the statistics (fig. S1 and Eq. 11 below). This is particularly important at high laser powers P where first-passage times become long. In practice, one should vary the interval of $\langle\tau_R\rangle$ to be fitted even if it appears to have a slope of two. Sampling of first-passage trajectories in a range of R values may be considered to be sufficient if the fitted d_f does not change upon increasing and decreasing said interval. The uncertainty (i.e., the error bars) of the fitted fractal dimension d_f in Figs. 2A and 3C was determined by repeating the fitting procedure 30 times on datasets obtained by randomly omitting 20% of the points.

Theory of the "outer" first-passage problem on fractals

We are interested in the time it takes a particle initially located at $\mathbf{R}(0)$ to reach a displacement R, i.e.

$$\tau_R \equiv \min_t\{|\mathbf{R}(t)-\mathbf{R}(0)| = R\} \tag{7}$$

Mathematically, the problem can be stated as the two-point boundary value problem for the probability density of the relative displacement $r(t) \equiv |\mathbf{R}(t) - \mathbf{R}(0)|$. The corresponding Green's function is governed by the backward Fokker-Planck equation (*4*, *5*)

$$[\partial_t - D r^{1-d_f}\partial_r r^{d_f-1}\partial_r] G(r,t|r_0) = 0 \tag{8}$$

with initial condition $G(r,0|r_0) = \delta(r-r_0)/\Omega_{d_f} r_0^{d_f-1}$ and boundary conditions

$$G(R,t|r_0) = 0,\ \partial_r G(r,t|r_0)|_{r=\epsilon} = 0, \text{ and } \forall t \tag{9}$$

where Ω_{d_f} is the hyperspherical solid angle. The reflecting boundary at $0 \le \epsilon \le r_0$ is required to assure well posedness of the Green's function. That is, we formally assume a fictitious infinitesimal radial shift of the initial condition $\mathbf{R}(0) \to \mathbf{R}(0) + \epsilon\hat{r}$. The first-passage time density $\wp(\tau_R)$ is obtained from the probability flux into the absorbing boundary at R. The problem is solved by Laplace transforming Eq. 8 in time $t \to s$, i.e., $\tilde{p}(r,s|0) = \int_0^\infty e^{-st} p(r,t|0)\,dt$, using the initial condition $p(r_0,0|r_0) = \delta(r-r_0)/\Omega_{d_f} r_0^{d_f-1}$ and solving for the resulting Green's function, where Ω_{d_f} is the d_f dimensional solid angle. Upon carefully taking the limits, first $\lim_{r_0\to\epsilon}$ and then $\lim_{\epsilon\to 0}$, we obtain

$$\tilde{\wp}(s) = \left(\frac{R}{2}\sqrt{\frac{s}{D}}\right)^{\nu}\left[\Gamma(1+\nu)\,I_\nu\left(R\sqrt{\frac{s}{D}}\right)\right]^{-1} \tag{10}$$

where we strictly assume the principal branch of $\sqrt{s}$, where $-1 < \nu = (d_f/2) - 1 \le 1/2$, and where $I_\nu(z)$ is the modified Bessel function of

the first kind of order ν. Using the identity relating the ordinary and modified Bessel functions, $I_\nu(z) = e^{-i\nu\pi/2} J_\nu(ze^{i\pi/2})$, and $\beta_{\nu,k}$, the tabulated k-th root of the Bessel function of order ν, $J_\nu(\beta_{\nu,k}) = 0$, we invert $\tilde{\wp}(s) \to \wp(\tau_R)$ by means of Cauchy's residue theorem to obtain the general exact result given in Eq. 2. To accommodate for subdiffusion with a mean squared displacement $\langle \delta R^2 \rangle = 2 d_f D_w t^{2/d_w}$, the above generalized diffusion operator must be changed to $D_w r^{1-d_f} \partial_r r^{1+d_f-d_w} \partial_r$. Accordingly, we must throughout make the replacements [see, e.g., (*20*, *32*)] $R/\sqrt{D} \to (2/d_w)\sqrt{R^{d_w}/D_w}$ and $\nu \to \mu = (d_f + 1)/d_w - 3/2$, which yields, after some straightforward calculations, Eqs. 5 and 6, respectively. In the case that the embedding space has Euclidean dimension d, we have $-3/2 < \mu \leq 1/2$.

To provide more intuition about Eq. 2, we further inspect the short- and long-time asymptotic behavior of the first-passage time density. The short-time asymptotics are nontrivial and follow from taking the limit $s \to \infty$ in Eq. 10 and inverting the resulting Laplace transform using the residue transfer theorem that yields

$$\lim_{\tau_R \to 0} \wp(\tau_R) = \frac{\sqrt{2}}{\Gamma(1+\nu)} \left(\frac{R}{2\sqrt{2D\tau_R}} \right)^{\nu+1/2} \frac{e^{-R^2/(8D\tau_R)}}{\tau_R} D_{\nu+3/2}\left(\frac{R}{\sqrt{2D\tau_R}} \right) \quad (11)$$

where $D_\mu(z)$ is the parabolic cylinder function. Equation 11 reflects the initial rise of $\wp(\tau_R)$ that is corroborated by the experimental data within the experimental time window and uncertainty (bottom left inset of Fig. 2B).

Conversely, the long-time asymptotics follow immediately from the leading term of the exact solution in Eq. 2

$$\lim_{\tau_R \to \infty} \wp(\tau_R) = \frac{4D}{R^2} \frac{(\beta_{\nu,1}/2)^{\nu+1}}{\Gamma(1+\nu) J_{\nu+1}(\beta_{\nu,1})} e^{-D\beta_{\nu,1}^2 \tau_R/R^2} \quad (12)$$

and are exponential. Therefore, if the experimental trajectories are sufficiently longer than $R^2/D\beta_{\nu,1}^2$, then the mean first-passage can be reliably determined without appreciable effects of the finiteness of trajectories.

Let us, lastly, inspect the effect of too short trajectories. More precisely, we inspect the effect of a temporal cutoff on the N-th moment of the first-passage time $\langle \tau_R^N \rangle$. For the sake of simplicity, we focus on $d_w = 2$; the extension to the subdiffusive scenario with $d_w > 2$ is straightforward. For trajectories of length T, the N-th moment of the "finite-time" first-passage time is given by

$$\begin{aligned} \langle \tilde{\tau}_R^N(T) \rangle &\equiv \frac{\int_0^T \tau_R^N \wp(\tau_R)\, d\tau_R}{\int_0^T \wp(\tau_R)\, d\tau_R} \\ &= \left(\frac{R^2}{D}\right)^N \frac{\sum_{k\geq 1} \beta_{\nu,k}^{\nu-1-2N} \gamma(N+1, DT\beta_{\nu,k}^2/R^2)/J_{\nu+1}(\beta_{\nu,k})}{\sum_{k\geq 1} \beta_{\nu,k}^{\nu-1}\left(1 - e^{-\beta_{\nu,k}^2 DT/R^2}\right)/J_{\nu+1}(\beta_{\nu,k})} \end{aligned} \quad (13)$$

where $\gamma(\alpha, z)$ denotes the lower incomplete Gamma function. In the limit of long trajectories $T \gg R^2/D\beta_{\nu,k}^2$, we recover for $N = 1$ the result in Eqs. 1 and 2 that depends quadratically on R. Conversely, for small values of T, the finite-time cutoff may change the behavior profoundly; in particular, it may give rise to a subquadratic scaling of $\langle \tilde{\tau}_R(T) \rangle$ in R (fig. S1). A minor finite-time cutoff preserves (within the statistical uncertainty of the experiment) the quadratic scaling in R but may lead to a slight overestimation of the bare diffusion coefficient D (see blue symbols in fig. S1C for $R/R_{max} < 0.5$). However, it does so for any laser power, and since d_f is determined by the ratio of the fitted prefactors, this is not expected to cause any major issues.

SUPPLEMENTARY MATERIALS

Supplementary material for this article is available at https://science.org/doi/10.1126/sciadv.abk0627

REFERENCES AND NOTES

1. B. B. Mandelbrot, *The Fractal Geometry of Nature* (W. H. Freeman and Comp., ed. 3, 1983).
2. D. Stauffer, A. Aharony, *Introduction to Percolation Theory* (Taylor & Francis, 1992).
3. D. ben Avraham and S. Havlin, *Diffusion and Reactions in Fractals and Disordered Systems* (Cambridge Univ. Press, 2000).
4. B. O'Shaughnessy, I. Procaccia, Analytical solutions for diffusion on fractal objects. *Phys. Rev. Lett.* **54**, 455–458 (1985).
5. B. O'Shaughnessy, I. Procaccia, Diffusion on fractals. *Phys. Rev. A* **32**, 3073–3083 (1985).
6. J. D. Hyman, M. Dentz, A. Hagberg, P. K. Kang, Emergence of stable laws for first passage times in three-dimensional random fracture networks. *Phys. Rev. Lett.* **123**, 248501 (2019).
7. J. W. Crawford, P. Baveye, P. Grindrod, C. Rappoldt, in *Assessment of Non-Point Source Pollution in the Vadose Zone*, *Application of fractals to soil properties, landscape patterns, and solute transport in porous media* (American Geophysical Union, 2013), p. 151.
8. A. B. Harris, A. Aharony, Anomalous diffusion, superlocalization and hopping conductivity on fractal media. *Europhys. Lett.* **4**, 1355–1360 (1987).
9. T. Ala-Nissila, S. Ying, Theory of classical surface diffusion. *Prog. Surf. Sci.* **39**, 227–323 (1992).
10. D. Ernst, J. Köhler, M. Weiss, Probing the type of anomalous diffusion with single-particle tracking. *Phys. Chem. Chem. Phys.* **16**, 7686–7691 (2014).
11. M. Weiss, M. Elsner, F. Kartberg, T. Nilsson, Anomalous subdiffusion is a measure for cytoplasmic crowding in living cells. *Biophys. J.* **87**, 3518–3524 (2004).
12. M. Weiss, H. Hashimoto, T. Nilsson, Anomalous protein diffusion in living cells as seen by fluorescence correlation spectroscopy. *Biophys. J.* **84**, 4043–4052 (2003).
13. Y. Golan, E. Sherman, Resolving mixed mechanisms of protein subdiffusion at the T cell plasma membrane. *Nat. Commun.* **8**, 15851 (2017).
14. A. Kusumi, C. Nakada, K. Ritchie, K. Murase, K. Suzuki, H. Murakoshi, R. S. Kasai, J. Kondo, T. Fujiwara, Paradigm shift of the plasma membrane concept from the two-dimensional continuum fluid to the partitioned fluid: High-speed single-molecule tracking of membrane molecules. *Annu. Rev. Biophys. Biomol. Struct.* **34**, 351–378 (2005).
15. A. Bancaud, S. Huet, N. Daigle, J. Mozziconacci, J. Beaudouin, J. Ellenberg, Molecular crowding affects diffusion and binding of nuclear proteins in heterochromatin and reveals the fractal organization of chromatin. *EMBO J.* **28**, 3785–3798 (2009).
16. A. Bancaud, C. Lavelle, S. Huet, J. Ellenberg, A fractal model for nuclear organization: Current evidence and biological implications. *Nucleic Acids Res.* **40**, 8783–8792 (2012).
17. S. Schoenfelder, P. Fraser, Long-range enhancer-promoter contacts in gene expression control. *Nat. Rev. Genet.* **20**, 437–455 (2019).
18. Y. Li, A. Eshein, R. K. A. Virk, A. Eid, W. Wu, J. Frederick, D. Van Derway, S. Gladstein, K. Huang, A. R. Shim, N. M. Anthony, G. M. Bauer, X. Zhou, V. Agrawal, E. M. Pujadas, S. Jain, G. Esteve, J. E. Chandler, T.-Q. Nguyen, R. Bleher, J. J. de Pablo, I. Szleifer, V. P. Dravid, L. M. Almassalha, V. Backman, Nanoscale chromatin imaging and analysis platform bridges 4D chromatin organization with molecular function. *Sci. Adv.* **7**, eabe4310 (2021).
19. T. Neusius, I. Daidone, I. M. Sokolov, J. C. Smith, Subdiffusion in peptides originates from the fractal-like structure of configuration space. *Phys. Rev. Lett.* **100**, 188103 (2008).
20. O. Bénichou, C. Chevalier, J. Klafter, B. Meyer, R. Voituriez, Geometry-controlled kinetics. *Nat. Chem.* **2**, 472–477 (2010).
21. C. Rabouille, S. Cortassa, M. A. Aon, Fractal organisation in biological macromolecular lattices. *J. Biomol. Struct. Dyn.* **9**, 1013–1024 (1992).
22. M. A. Aon, S. Cortassa, On the fractal nature of cytoplasm. *FEBS Lett.* **344**, 1–4 (1994).
23. A. L. Mehaute, G. Crepy, Introduction to transfer and motion in fractal media: The geometry of kinetics. *Solid State Ionics* **9-10**, 17 (1983).
24. H. D. Ou, S. Phan, T. J. Deerinck, A. Thor, M. H. Ellisman, C. C. O'Shea, Chromemt: Visualizing 3D chromatin structure and compaction in interphase and mitotic cells. *Science* **357**, eaag0025 (2017).
25. A. N. Boettiger, B. Bintu, J. R. Moffitt, S. Wang, B. J. Beliveau, G. Fudenberg, M. Imakaev, L. A. Mirny, C.-t. Wu, X. Zhuang, Super-resolution imaging reveals distinct chromatin folding for different epigenetic states. *Nature* **529**, 418–422 (2016).
26. B. Bintu, L. J. Mateo, J.-H. Su, N. A. Sinnott-Armstrong, M. Parker, S. Kinrot, K. Yamaya, A. N. Boettiger, X. Zhuang, Super-resolution chromatin tracing reveals domains and cooperative interactions in single cells. *Science* **362**, eaau1783 (2018).
27. L. M. Almassalha, G. M. Bauer, W. Wu, L. Cherkezyan, D. Zhang, A. Kendra, S. Gladstein, J. E. Chandler, D. VanDerway, B.-L. L. Seagle, A. Ugolkov, D. D. Billadeau, T. V. O'Halloran, A. P. Mazar, H. K. Roy, I. Szleifer, S. Shahabi, V. Backman, Macrogenomic engineering via modulation of the scaling of chromatin packing density. *Nat. Biomed. Eng.* **1**, 902–913 (2017).

28. J. Moller, J. J. de Pablo, Bottom-up meets top-down: The crossroads of multiscale chromatin modeling. *Biophys. J.* **118**, 2057–2065 (2020).
29. Y. Meroz, I. M. Sokolov, J. Klafter, Test for determining a subdiffusive model in ergodic systems from single trajectories. *Phys. Rev. Lett.* **110**, 090601 (2013).
30. Y. Meroz, I. M. Sokolov, A toolbox for determining subdiffusive mechanisms. *Phys. Rep.* **573**, 1–29 (2015).
31. R. Metzler, J.-H. Jeon, A. G. Cherstvy, E. Barkai, Anomalous diffusion models and their properties: Non-stationarity, non-ergodicity, and ageing at the centenary of single particle tracking. *Phys. Chem. Chem. Phys.* **16**, 24128–24164 (2014).
32. A. Godec, R. Metzler, Universal proximity effect in target search kinetics in the few-encounter limit. *Phys. Rev. X* **6**, 041037 (2016).
33. D. Hartich, A. Godec, Duality between relaxation and first passage in reversible markov dynamics: Rugged energy landscapes disentangled. *New J. Phys.* **20**, 112002 (2018).
34. D. Hartich, A. Godec, Interlacing relaxation and first-passage phenomena in reversible discrete and continuous space markovian dynamics. *J. Stat. Mech. Theor. Exp.* **2019**, 024002 (2019).
35. D. Hartich, A. Godec, Extreme value statistics of ergodic Markov processes from first passage times in the large deviation limit. *J. Phys. A Math. Theor.* **52**, 244001 (2019).
36. Y. Meroz, I. M. Sokolov, J. Klafter, Unequal twins: Probability distributions do not determine everything. *Phys. Rev. Lett.* **107**, 260601 (2011).
37. S. Condamin, V. Tejedor, R. Voituriez, O. Bénichou, J. Klafter, Probing microscopic origins of confined subdiffusion by first-passage observables. *Proc. Natl. Acad. Sci. U.S.A.* **105**, 5675–5680 (2008).
38. J. Gladrow, M. Ribezzi-Crivellari, F. Ritort, U. F. Keyser, Experimental evidence of symmetry breaking of transition-path times. *Nat. Commun.* **10**, 55 (2019).
39. A. L. Thorneywork, J. Gladrow, Y. Qing, M. Rico-Pasto, F. Ritort, H. Bayley, A. B. Kolomeisky, U. F. Keyser, Direct detection of molecular intermediates from first-passage times. *Sci. Adv.* **6**, eaaz4642 (2020).
40. S. C. Weber, A. J. Spakowitz, J. A. Theriot, Bacterial chromosomal loci move subdiffusively through a viscoelastic cytoplasm. *Phys. Rev. Lett.* **104**, 238102 (2010).
41. H. Löwen, Colloidal dispersions in external fields: Recent developments. *J. Phys.* **20**, 404201 (2008).
42. F. Evers, R. D. L. Hanes, C. Zunke, R. F. Capellmann, J. Bewerunge, C. Dalle-Ferrier, M. C. Jenkins, I. Ladadwa, A. Heuer, R. Castañeda-Priego, S. U. Egelhaaf, Colloids in light fields: Particle dynamics in random and periodic energy landscapes. *Eur. Phys. J. Special Topics* **222**, 2995–3009 (2013).
43. G. Volpe, G. Volpe, S. Gigan, Brownian motion in a speckle light field: Tunable anomalous diffusion and selective optical manipulation. *Sci. Rep.* **4**, 3936 (2014).
44. A. Ashkin, Optical trapping and manipulation of neutral particles using lasers. *Proc. Natl. Acad. Sci.* **94**, 4853–4860 (1997).
45. D. G. Grier, A revolution in optical manipulation. *Nature* **424**, 810–816 (2003).
46. I. A. Martínez, E. Roldán, L. Dinis, D. Petrov, J. M. R. Parrondo, R. A. Rica, Brownian carnot engine. *Nat. Phys.* **12**, 67–70 (2015).
47. N. Osterman, I. Poberaj, J. Dobnikar, D. Frenkel, P. Ziherl, D. Babic, Field-induced self-assembly of suspended colloidal membranes. *Phys. Rev. Lett.* **103**, 228301 (2009).
48. R. M. Erb, H. S. Son, B. Samanta, V. M. Rotello, B. B. Yellen, Magnetic assembly of colloidal superstructures with multipole symmetry. *Nature* **457**, 999–1002 (2009).
49. A. Yethiraj, Tunable colloids: Control of colloidal phase transitions with tunable interactions. *Soft Matter* **3**, 1099–1115 (2007).
50. A. Terray, J. Oakey, D. W. M. Marr, Microfluidic control using colloidal devices. *Science* **296**, 1841–1844 (2002).
51. J. W. Goodman, *Speckle Phenomena in Optics: Theory and Applications* (SPIE, ed. 2, 2020).
52. J. Bewerunge, S. U. Egelhaaf, Experimental creation and characterization of random potential-energy landscapes exploiting speckle patterns. *Phys. Rev. A* **93**, 013806 (2016).
53. G. Volpe, L. Kurz, A. Callegari, G. Volpe, S. Gigan, Speckle optical tweezers: Micromanipulation with random light fields. *Opt. Express* **22**, 18159–18167 (2014).
54. J. Bewerunge, A. Sengupta, R. F. Capellmann, F. Platten, S. Sengupta, S. U. Egelhaaf, Colloids exposed to random potential energy landscapes: From particle number density to particle-potential and particle-particle interactions. *J. Chem. Phys.* **145**, 044905 (2016).
55. S. Guyot, M.-C. Péron, E. Deléchelle, Spatial speckle characterization by Brownian motion analysis. *Phys. Rev. E* **70**, 046618 (2004).
56. J. C. Crocker, D. G. Grier, Methods of digital video microscopy for colloidal studies. *J. Colloid Interface Sci.* **179**, 298–310 (1996).
57. J. Bewerunge, I. Ladadwa, F. Platten, C. Zunke, A. Heuer, S. U. Egelhaaf, Time- and ensemble-averages in evolving systems: The case of Brownian particles in random potentials. *Phys. Chem. Chem. Phys.* **18**, 18887–18895 (2016).
58. F. Evers, C. Zunke, R. D. L. Hanes, J. Bewerunge, I. Ladadwa, A. Heuer, S. U. Egelhaaf, Particle dynamics in two-dimensional random-energy landscapes: Experiments and simulations. *Phys. Rev. E* **88**, 022125 (2013b).
59. P. M. H. Lee, B. D. Hughes, *Random walks and random environments: Volume 1: Random walks* (Clarendon Press, 1995).
60. H. Faxén, Der Widerstand gegen die Bewegung einer starren Kugel in einer zähen Flüssigkeit, die zwischen zwei parallelen ebenen Wänden eingeschlossen ist. *Ann. Phys.* **373**, 89–119 (1922).
61. P. Sharma, S. Ghosh, S. Bhattacharya, A high-precision study of hindered diffusion near a wall. *Appl. Phys. Lett.* **97**, 104101 (2010).
62. A. D. Ducharme, G. D. Boreman, D. R. Snyder, Effects of intensity thresholding on the power spectrum of laser speckle. *Appl. Opt.* **33**, 2715–2720 (1994).
63. D. S. Dean, I. T. Drummond, R. R. Horgan, Effective transport properties for diffusion in random media. *J. Stat. Mech.* **2007**, P07013 (2007).
64. D. Hartich, A. Godec, Thermodynamic uncertainty relation bounds the extent of anomalous diffusion. *Phys. Rev. Lett.* **127**, 080601 (2021).
65. M. Kampmann, Facilitated diffusion in chromatin lattices: Mechanistic diversity and regulatory potential. *Mol. Microbiol.* **57**, 889–899 (2005).
66. O. Bénichou, C. Chevalier, B. Meyer, R. Voituriez, Facilitated diffusion of proteins on chromatin. *Phys. Rev. Lett.* **106**, 038102 (2011).
67. R. Cortini, G. J. Filion, Theoretical principles of transcription factor traffic on folded chromatin. *Nat. Commun.* **9**, 1740 (2018).
68. P. Fraser, W. Bickmore, Nuclear organization of the genome and the potential for gene regulation. *Nature* **447**, 413–417 (2007).
69. M. Wachsmuth, W. Waldeck, J. Langowski, Anomalous diffusion of fluorescent probes inside living cell nuclei investigated by spatially-resolved fluorescence correlation spectroscopy. *J. Mol. Biol.* **298**, 677–689 (2000).
70. M. Platani, I. Goldberg, A. I. Lamond, J. R. Swedlow, Cajal body dynamics and association with chromatin are ATP-dependent. *Nat. Cell Biol.* **4**, 502–508 (2002).
71. J. W. Crawford, N. Matsui, Heterogeneity of the pore and solid volume of soil: Distinguishing a fractal space from its non-fractal complement. *Geoderma* **73**, 183–195 (1996).
72. J. P. Segovia-Gutiérrez, M. A. Escobedo-Sánchez, E. Sarmiento-Gómez, S. U. Egelhaaf, Diffusion of anisotropic particles in random energy landscapes–an experimental study. *Front. Phys.* **7**, 224 (2020).
73. C. Bechinger, R. Di Leonardo, H. Löwen, C. Reichhardt, G. Volpe, G. Volpe, Active particles in complex and crowded environments. *Rev. Mod. Phys.* **88**, 045006 (2016).
74. J. Schwarz-Linek, J. Arlt, A. Jepson, A. Dawson, T. Vissers, D. Miroli, T. Pilizota, V. A. Martinez, W. C. Poon, *Escherichia coli* as a model active colloid: A practical introduction. *Colloids Surf. B* **137**, 2–16 (2016).
75. J. Elgeti, R. G. Winkler, G. Gompper, Physics of microswimmers–single particle motion and collective behavior: A review. *Rep. Prog. Phys.* **78**, 056601 (2015).
76. J. Staforelli, J. Brito, E. Vera, P. Solano, A. Lencina, A clustered speckle approach to optical trapping. *Opt. Commun.* **283**, 4722–4726 (2010).
77. O. Carvalho, B. Clairac, M. Benderitter, L. Roy, Statistical speckle study to characterize scattering media: Use of two complementary approaches. *Opt. Express* **15**, 13817–13831 (2007).

Acknowledgments: We acknowledge fruitful discussions with M. Weiss and R. Metzler. **Funding:** We acknowledge financial support from the German Research Foundation (DFG) through the Emmy Noether Programme GO 2762/1-1 (to A.G.) and grant EG269/6-1 (to S.U.E.).
Author contributions: S.U.E. and A.G. conceived the research and drafted the manuscript. J.B., C.Z., and F.P. performed the experiments, and A.G. performed the theoretical calculations. All authors contributed to the analysis of the data, the interpretation of the results, and the writing of the manuscript. **Competing interests:** The authors declare that they have no competing interests. **Data and materials availability:** All data needed to evaluate the conclusions in the paper are present in the paper and/or the Supplementary Materials.

Submitted 13 July 2021
Accepted 29 November 2021
Published 21 January 2022
10.1126/sciadv.abk0627

First-passage statistics of colloids on fractals: Theory and experimental realization

Christoph ZunkeJörg BewerungeFlorian PlattenStefan U. EgelhaafAljaž Godec

Sci. Adv., 8 (3), eabk0627. • DOI: 10.1126/sciadv.abk0627